# Exclusive dielectron production in ultraperipheral Pb+Pb collisions at $\sqrt{s_{\mathrm{NN}}}$ = 5.02 TeV with ATLAS

## The ATLAS Collaboration

Exclusive production of dielectron pairs, $\gamma\gamma \to e^+e^-$, is studied using $\mathcal{L}_{\mathrm{int}}$ = 1.72 nb$^{-1}$ of data from ultraperipheral collisions of lead nuclei at $\sqrt{s_{\mathrm{NN}}}$ = 5.02 TeV recorded by the ATLAS detector at the LHC. The process of interest proceeds via photon-photon interaction in the strong electromagnetic fields of relativistic lead nuclei. Dielectron production is measured in the fiducial region defined by following requirements: electron transverse momentum, $p_{\mathrm{T}}^e$ > 2.5 GeV, absolute electron pseudorapidity, $|\eta^e|$ < 2.5, invariant mass of the dielectron system, $m_{ee}$ > 5 GeV, and transverse momentum of the dielecton pair, $p_{\mathrm{T}}^{ee}$ < 2 GeV. Differential cross-sections are measured as a function of $m_{ee}$, average $p_{\mathrm{T}}^e$, absolute rapidity of the dielectron system, $|y_{ee}|$, and scattering angle in the dielectron rest frame, $|\cos\theta^*|$, in the inclusive sample, and also under the requirement of no activity in the forward direction. The total integrated fiducial cross-section is measured to be 215 $\pm$1 (stat.) $^{+23}_{-20}$ (syst.) $\pm$4 (lumi.) $\mu$b. Within experimental uncertainties the measured integrated cross-section is in good agreement with the QED predictions from the Monte Carlo programs Starlight and SuperChic, confirming the broad features of the initial photon fluxes. The differential cross-sections show systematic differences with these predictions which are more pronounced at high $|y_{ee}|$ and $|\cos\theta^*|$ values.

# 1 Introduction

Collisions of ultrarelativistic heavy ions provide an opportunity to study not only the strong interactions between nucleons but also processes involving electromagnetic (EM) interactions. This is due to the presence of intense EM fields associated with the ultrarelativistic ions. The EM interactions become dominant at large impact parameters, $b > 2R_A$, where $R_A$ is the ion radius. Such collisions are usually referred to as ultraperipheral collisions (UPC). Comprehensive reviews of UPC physics can be found in Refs. [1, 2].

The EM fields associated with the ultrarelativistic nuclei can be treated as fluxes of quasi-real photons according to the equivalent photon approximation (EPA) formalism [3, 4]. In this approach, the total cross-section for a given process is calculated as a convolution of the photon flux with the elementary production cross-section. Although the same approach is also valid for proton-proton ($pp$) collisions, the expected cross-sections are strongly enhanced in the heavy-ion (HI) collisions. The photon flux from each nucleus is enhanced by a factor of $Z^2$, where $Z$ is the atomic number. That results in $Z^4$ enhancement of the cross-sections. For lead (Pb, $Z = 82$) this $Z^4$ enhancement is $4.5 \times 10^7$. Another advantage of studying photon-induced interactions in UPC HI collisions is the relatively low number of interactions per LHC bunch crossing. The mean number of simultaneous interactions, $\mu$, is typically at subpercent level. This provides a clean environment, facilitating the detection of the interaction products, and little contamination from unrelated interactions in the same crossing. With the centre-of-mass energy per nucleon pair available at the Large Hadron Collider (LHC), $\sqrt{s_{NN}}$ = 5.02 TeV, the initial photons can reach energies up to 75–100 GeV.

Among the possible set of photon-induced reactions, the exclusive production of dielectron pairs from photon-photon collisions, i.e. $\gamma\gamma \to e^+e^-$, is one of the cleanest elementary processes. This process, also referred to as the Breit-Wheeler process [5], is a non-resonant two-photon scattering to opposite-charged electron pairs. The outgoing nuclei may be excited, for example via the giant dipole resonance [6]. A Feynman diagram of the leading-order $\gamma\gamma \to e^+e^-$ reaction is shown in Figure 1. Even for large $\gamma\gamma$



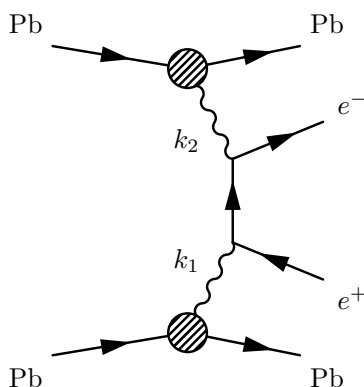Figure 1: Feynman diagram of leading order $\gamma\gamma \to e^+e^-$ process.

invariant masses, the relatively large cross-section associated with this process allows for precise differential measurements. Thus, this process is a particularly effective tool for studying the modeling of photon fluxes and elementary production cross-sections, as well as for studying the effects of nuclear breakup, whose probability is strongly correlated with the internuclear impact parameter [2]. The nuclear breakup gives

rise to the forward neutron production and the larger fraction of events with such activity is present at smaller impact parameters.

Exclusive dilepton production, via both electron pair and muon pair final states, has been measured by ATLAS and CMS in $pp$ collisions at $\sqrt{s}$ = 7 TeV [7–9] and $\sqrt{s}$ = 13 TeV [10–12]. The ALICE Collaboration measured exclusive production of electron pairs in Pb+Pb collisions at $\sqrt{s_{NN}}$ = 2.76 TeV [13] over a limited kinematic range. The STAR experiment at RHIC has measured exclusive dileptons at lower invariant masses at $\sqrt{s_{NN}}$ = 200 GeV for both Au+Au and U+U collisions [14, 15]. With the higher centre-of-mass energy of $\sqrt{s_{NN}}$ = 5.02 TeV, ATLAS performed differential measurements of $\gamma\gamma \to \mu^+\mu^-$ production in UPC Pb+Pb collisions [16]. Both STAR and ATLAS observed substantial broadening of angular distributions for exclusive dileptons from $\gamma\gamma$ interactions in events where the nuclei overlapped and interacted hadronically [14, 17]. Finally, CMS has observed that angular correlations in exclusive dimuon events were broadened significantly as a function of the impact parameter [18], as inferred by the amount of forward neutron production.

Exclusive dielectron production is an important reference process for other measurements. Ref. [19] and [20] proposed using it in the context of $\gamma\gamma \to \tau^+\tau^-$ production, in order to reduce the impact of correlated systematic uncertainties for the measurement of the $\tau$-lepton anomalous magnetic moment. It is also an important background for light-by-light scattering, which proceeds via loop diagrams and thus has a much lower cross-section. This was assessed in several publications on light-by-light scattering by both ATLAS [21–23] and CMS [24].

In this note, a measurement of the exclusive production of dielectrons with the ATLAS detector at the LHC is presented. It uses Pb+Pb data collected in 2018 which brings a factor of three improvement in an integrated luminosity compared to the ATLAS dimuon measurement [16]. Dielectron production is measured in the fiducial region defined by the following requirements: electron transverse momentum $p_T^e$ > 2.5 GeV, electron pseudorapidity $|\eta^e|$ < 2.5, invariant mass $m_{ee}$ > 5 GeV, and dielectron transverse momentum $p_T^{ee}$ < 2 GeV. This fiducial region has a wider coverage in the minimum lepton $p_T$ and invariant mass of the dilepton system by 1.5 and 5 units, respectively. The backgrounds originating from single-dissociative processes, Upsilon $\Upsilon(nS)$ production, and exclusive ditau production, $\gamma\gamma \to \tau^+\tau^-$, are estimated and subtracted. Differential cross-sections are measured as a function of $m_{ee}$, average electron transverse momentum ($\langle p_T^e \rangle$), absolute rapidity of the dielectron system $|y_{ee}|$, and scattering angle in the dielectron rest frame, $|\cos\theta^*|$. They are extracted inclusive in forward neutron activity, and in $\gamma\gamma \to e^+e^-$ events w/o activity in the forward direction. The latter is a unique feature of this analysis.

## 2 ATLAS detector

The ATLAS detector [25] at the LHC covers nearly the entire solid angle around the collision point. It consists of an inner tracking detector surrounded by a thin superconducting solenoid, electromagnetic and hadronic calorimeters, and a muon spectrometer incorporating three large superconducting toroidal magnets with eight coils each.

The inner-detector system (ID) is immersed in a 2 T axial magnetic field and provides charged particle tracking in the pseudorapidity range $|\eta|$ < 2.5 [1]. The high-granularity silicon pixel (Pixel) detector covers

---

[1] ATLAS uses a right-handed coordinate system with its origin at the nominal interaction point (IP) in the centre of the detector and the $z$-axis along the beam pipe. The $x$-axis points from the IP to the centre of the LHC ring, and the $y$-axis points upwards. Cylindrical coordinates $(r, \phi)$ are used in the transverse plane, $\phi$ being the azimuthal angle around the $z$-axis. The pseudorapidity

the vertex region which typically provides four measurements per track, with the first hit being normally in the Insertable B-Layer (IBL) [26], which was installed at the mean distance of 3.3 cm from the beam pipe before the start of Run 2. It is followed by the silicon microstrip tracker (SCT), which usually provides four two-dimensional measurement points per track. These silicon detectors are complemented by the transition radiation tracker, which enables radially extended track reconstruction up to $|\eta| = 2.0$.

The calorimeter system covers the pseudorapidity range $|\eta| < 4.9$. Within the region $|\eta| < 3.2$, electromagnetic calorimetry is provided by barrel and endcap lead/liquid-argon (LAr) calorimeters (high-granularity for $|\eta| < 2.5$), with an additional thin LAr presampler covering $|\eta| < 1.8$ to correct for energy loss in material upstream of the calorimeters. Hadronic calorimetry is provided by the steel/scintillating-tile calorimeter, which are segmented into three barrel structures within $|\eta| < 1.7$, and two copper/LAr hadronic endcap calorimeters. The solid angle coverage is completed with forward copper/LAr and tungsten/LAr calorimeter modules (FCal) optimised for electromagnetic and hadronic measurements respectively.

The muon spectrometer (MS) comprises separate trigger and high-precision tracking chambers measuring the deflection of muons in a magnetic field generated by superconducting air-core toroids. The precision chamber system covers the region $|\eta| < 2.7$ with three layers of monitored drift tubes, complemented by cathode strip chambers in the forward region, where the background is highest. The muon trigger system covers the range $|\eta| < 2.4$ with resistive plate chambers in the barrel, and thin gap chambers in the endcap regions.

The zero degree calorimeters (ZDC) consist of four longitudinal compartments on each side of the IP, each with one nuclear interaction length of tungsten absorber, with the Cherenkov light read out by 1.5 mm quartz rods. The detectors are located 140 m from the nominal IP in both directions, covering $|\eta| > 8.3$, and are well suited to measure neutral particles originating from the collision. In Pb+Pb collisions the ZDC allows for the detection of individual neutrons originating from the incoming nuclei. The ZDC calibration is performed in each set of four modules using photonuclear processes that deposit one or more neutrons on one side, and a single neutron, carrying the full per-nucleon beam energy, on the other. Time-dependent weights are determined for each module in short time intervals to minimize the variance around the nominal per-nucleon beam energy. Energy resolutions achieved are typically around $\Delta E/E \approx 16\%$.

The ATLAS trigger system [27, 28] consists of a Level-1 trigger implemented using a combination of dedicated electronics and programmable logic, and a software-based high-level trigger (HLT). An extensive software suite [29] is used in the reconstruction and analysis of real and simulated data, in detector operations, and in the trigger and data acquisition systems of the experiment.

# 3  Data and Monte Carlo simulation samples

The data used in this measurement is from Pb+Pb collisions with a centre-of-mass energy of $\sqrt{s_{\mathrm{NN}}} = 5.02$ TeV, recorded in 2018 with the ATLAS detector at the LHC. The full data set corresponds to an integrated luminosity of 1.72 nb$^{-1}$. Only high-quality data [30] with all detectors operating normally are analysed.

Monte Carlo (MC) simulated events for the $\gamma\gamma \rightarrow e^+e^-$ signal process were generated at leading order (LO) using STARLIGHT v313 [31]. In this approach, the cross-section is computed by convolving the Pb+Pb

---

is defined in terms of the polar angle $\theta$ as $\eta = -\ln\tan(\theta/2)$. Angular distance is measured in units of $\Delta R \equiv \sqrt{(\Delta\eta)^2 + (\Delta\phi)^2}$. The photon (electron) transverse energy is $E_{\mathrm{T}} = E/\cosh(\eta)$, where $E$ is its energy.

photon flux with the LO calculation for the elementary $\gamma\gamma \rightarrow e^+e^-$ process. The photon spectrum is calculated in impact parameter space by integrating the photon number density over all impact parameters under the assumption that the beam projectiles do not interact hadronically. This is done by utilizing a simple Glauber model [32] which provides an impact-parameter-dependent probability of inelastic processes. STARLIGHT also requires that the dilepton pairs are not formed within either nucleus. Several signal samples were produced for exclusive $m_{ee}$ ranges from $4.5 < m_{ee} < 200$ GeV. An alternative sample for the signal $\gamma\gamma \rightarrow e^+e^-$ process uses the SUPERCHIC v3.05 [33] programme. The difference between the nominal and alternative signal prediction is mainly in the implementation of the non-hadronic overlap condition of the Pb ions. In SUPERCHIC the probability for exclusive $\gamma\gamma \rightarrow e^+e^-$ interactions turns on smoothly for Pb+Pb impact parameters in the range of 15–20 fm and it is unity for larger values.

Backgrounds from $\gamma\gamma \rightarrow \tau^+\tau^-$ and $\Upsilon(nS) \rightarrow e^+e^-$ are also simulated using STARLIGHT v313. All generated events utilize PYTHIA8 (Py8) [34] to model QED final-state radiation (FSR) from the outgoing leptons.

Background contributions from exclusive dielectron production where either (single dissociation) or both (double dissociation) nuclei interact inelastically and dissociate were modelled using SUPER-CHIC v4.0 (SC4) [35]. It is interfaced to PYTHIA8 for showering and hadronisation. Since simulation of this process is only available for $pp$ collisions, a data-driven approach, discussed in detail in Sec. 5, is used in the analysis to utilise this sample in Pb+Pb collisions.

Apart from the alternative signal sample, all generated events are processed with a GEANT4 [36] based detector simulation [37] and are reconstructed with the standard ATLAS reconstruction software [29]. The alternative signal sample is used for comparisons with the measured differential cross-sections discussed in Section 8.

# 4 Signal selection and detector corrections

Candidate dielectron events were recorded using a dedicated trigger for events with moderate activity in the calorimeter but little additional activity in the entire detector. A logical OR of two Level-1 conditions was required: (1) at least one EM cluster with $E_T > 1$ GeV in coincidence with total $E_T$ registered in the calorimeter between 4–200 GeV, or (2) at least two EM clusters with $E_T > 1$ GeV with total $E_T$ registered in the calorimeter below 50 GeV. At the HLT level, a requirement on the total $E_T$ on each side of the FCal detector to be below 3 GeV was imposed. Additionally, a veto condition on the maximum activity in the Pixel detector, hereafter referred to as the Pixel-veto, had to be satisfied at the HLT level. The number of hits was required to be at most 15 to be compatible with low-multiplicity UPC events.

Electrons are reconstructed from EM clusters in the calorimeter and tracking information provided by the ID [38]. Selection requirements are applied to remove EM clusters with a large amount of energy from poorly functioning calorimeter cells, and a timing requirement is made to reject out-of-time candidates. An energy calibration specifically optimised for electrons and photons [38] is applied to the candidates to account for upstream energy loss and both lateral and longitudinal shower leakage. The calibration is derived for nominal $pp$ collisions with dedicated factors applied to account for the much lower contribution from multiple Pb+Pb collisions at the same bunch crossing.

The electron identification in this analysis is based on a loose cut-based working point [38] which is defined using selections on the shower-shape and tracking variables. Only electrons with $p_T^e > 2.5$ GeV and $|\eta^e| < 2.47$, excluding the calorimeter transition region $1.37 < |\eta^e| < 1.52$, are considered. The minimum

$p_T^e$ requirement is driven by the electron reconstruction efficiency which drops below 20% for $p_T^e$ values below this threshold.

Preselected events are required to have exactly two opposite-charge electrons satisfying the above selection criteria, with a dielectron invariant mass, $m_{ee}$, greater than 5 GeV. To suppress non-exclusive backgrounds, only two charged-particle tracks [39, 40] each with $p_T > 100$ MeV, $|\eta| < 2.5$, at least seven hits in the Pixel and SCT detectors in total and at most two silicon sensors without a hit, and associated with the dielectron system are allowed. To reject non-collision backgrounds such as cosmic-ray muons, no tracks in the MS system can be present in the event. Finally, the total $p_T$ of the dielectron system, $p_T^{ee}$, is required to be less than 2 GeV. Low $p_T^{ee}$ values are a key feature of the purely EM process which involves very low $p_T$ of the initial-state photons.

Each of the events passing the $\gamma\gamma \rightarrow e^+e^-$ criteria can be further classified into one of three categories based on the observed activity in the ZDC detector: 1) no neutron is registered in either ZDC ("0n0n"), 2) one or more forward neutrons registered in one ZDC and none in the other ("Xn0n"), and 3) one or more forward neutrons detected in both ZDC arms ("XnXn"). The observed fractions of events falling to these categories are: $f_{0n0n} = (62.9 \pm 0.3)\%$, $f_{Xn0n} = (29.7 \pm 0.3)\%$, and $f_{XnXn} = (7.4 \pm 0.2)\%$. Due to relatively large instantaneous luminosity of Pb+Pb collisions, which peaked around $7 \times 10^{27}$ cm$^{-2}$s$^{-1}$, additional neutrons might be generated per bunch crossing that are detected in one or both arms of the ZDC but are not associated with the exclusive dielectron process. This leads to an outflow from the 0n0n and Xn0n events to both the Xn0n and XnXn events. This effect is accounted for using the method established in Ref. [16]. The matrix equation with two fundamental parameters representing probabilities for having additional neutrons on one or both sides of the ZDC is built. The corrected fractions are measured in four bins of $m_{ee}$, with boundaries at 5, 10, 20, and 40 GeV and three bins of $|y_{ee}|$, with boundaries at 0, 0.8, 1.6, and 2.4, and also in the sample integrated in $m_{ee}$ and $|y_{ee}|$. On average they are larger by about 13% compared to the observed fractions. Figure 2 shows the fractions of events in the 0n0n category in four bins of $m_{ee}$ and three bins of $|y_{ee}|$, corrected for the presence of additional neutrons. These fractions tend to drop with increasing mass, and are in general larger for higher $|y_{ee}|$ values. The only point that does not follow this scheme is the bin with highest $m_{ee}$ and $|y_{ee}|$, but it also has the largest statistical uncertainty. For the rapidity range of $|y_{ee}| < 0.8$, which has the largest number of events, the $f_{0n0n}$ values drop from about 78% in the lowest mass bin to about 57% in the highest mass bin. The systematic uncertainties on the fractions of events in the 0n0n category originate from a few sources: uncertainties on the measured exclusive single and mutual EM dissociation probabilities by the ALICE Collaboration [41], and their extrapolation from $\sqrt{s_{NN}} = 2.76$ TeV to 5.02 TeV as evaluated in Ref. [16], the uncertainty on the dissociative background contribution as discussed in Section 5, and uncertainty on ZDC efficiency.

The efficiency of the primary physics trigger ($\epsilon_T$) is determined as $\epsilon_T = \varepsilon_{L1} \cdot \varepsilon_{PixVeto} \cdot \varepsilon_{FCal}$, where $\varepsilon_{L1}$ is the efficiency of the Level-1 EM trigger to register the moderate calorimeter activity characteristic for the signal process, $\varepsilon_{PixVeto}$ is the efficiency of the trigger to reject events with large numbers of Pixel detector hits, and $\varepsilon_{FCal}$ is the efficiency of the FCal selection to reject events with large energy depositions on either side. Individual efficiencies are evaluated using a sample of $\gamma\gamma \rightarrow e^+e^-$ events collected using a set of dedicated supporting triggers that each do not reject events based on the condition under study in the primary physics trigger. The $\varepsilon_{L1}$ rises with the sum of the transverse energies of the two electron clusters and reaches 100% for $\Sigma E_T > 8$ GeV. The Pixel-veto efficiency is measured as a function of the dielectron rapidity and is just over 80% for $|y_{ee}| \sim 0$ and falls to about 50% for $|y_{ee}| > 2$. The dependence on $|y_{ee}|$ originates from a growing number of Pixel-detector layers in the forward direction which a dielectron pair has to pass. Finally, the FCal veto efficiency is measured to be $(99.1 \pm 0.6)\%$, and it is constant for the entire range in $\Sigma E_T$. The total uncertainty in the trigger efficiency is determined by varying all of the
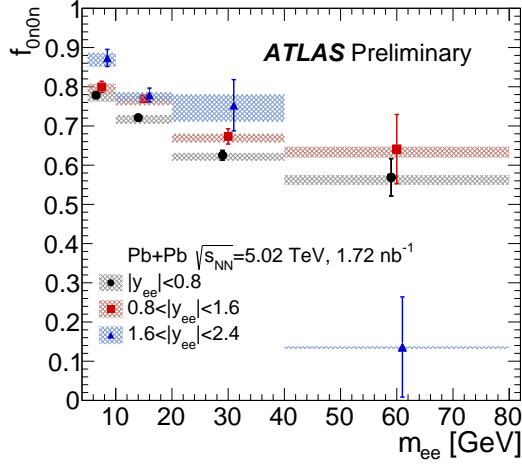
6

Figure 2: Fractions of events in the 0n0n category evaluated from data in three bins of $|y_{ee}|$, corrected for the presence of additional neutrons. Error bars represent statistical uncertainties, while shaded boxes represent systematic uncertainties. Points for $|y_{ee}| < 0.8$ and $1.6 < |y_{ee}| < 2.4$ are displaced horizontally for better visibility.

individual components up and down by their respective total uncertainties. They amount to about 3–4% for the primary calorimeter pair trigger, driven mainly by the limited number of events collected by an independent trigger of the dielectron sample, and less than a percent for the other contributions.

The total electron efficiency is a product of the electron reconstruction efficiency and the loose electron identification efficiency [38]. This is determined in data using a sample of events triggered by the presence of EM clusters, limited total $E_{\mathrm{T}}$, and a maximal number of Pixel hits, on which a tag-and-probe procedure is used. The tag is a well reconstructed, high-purity electron candidate with $E_{\mathrm{T}} > 2.5$ GeV, and the probe is an opposite-charge track built from the Pixel detector (referred to as "Pixel-track") with at least 3 hits. The invariant mass of the tag and probe system must exceed 5 GeV and the acoplanarity ($\alpha = 1 - \frac{|\Delta\phi|}{\pi}$, where $\Delta\phi$ is a difference in the azimuthal angle of two electrons) has to be less than 0.1. The extracted mass distribution is found to agree well with a reconstructed sample of STARLIGHT events. The reconstruction efficiency is defined as a fraction of probes which are reconstructed electrons, while the identification efficiency is a fraction of reconstructed electrons which are identified as loose electrons. The reconstruction efficiency has large variations with both $p_{\mathrm{T}}$ and Pixel-track $\eta$ and ranges from about 30% at $p_{\mathrm{T}} = 2.5$ GeV to 95% above 15 GeV. The identification efficiency is found to vary more weakly with Pixel-track $\eta$ between 80 and 90%. Then, the total reconstruction scale factors are extracted as a ratio of efficiencies measured in data over MC simulation. They vary between 0.9 and 1.2 with the largest deviations from unity in the forward direction for absolute Pixel-track $\eta$ above 1.1. Systematic uncertainties on the scale factors are evaluated using the tighter selection criteria on the tag and probe candidates, as well as reducing a potential contribution from background processes by limiting the measurement to the 0n0n category or to a narrow acoplanarity region $\alpha < 0.01$. The total systematic uncertainty is at the level of 5% at central Pixel-track $|\eta| < 1$ values, while it grows to 10% in the forward direction. In the forward region, the magnitude of statistical and systematic uncertainties is comparable.

# 5 Background contributions

There are three primary sources of backgrounds considered in this analysis, presented in order of their magnitude: dissociative electron pair production where one or both photons are emitted from a resolved nucleon, and not coherently from the whole nucleus, Upsilon production, and exclusive $\tau$-lepton pair (ditau) production.

The largest source of background originates from $\gamma\gamma \to e^+e^-$ production with nuclear dissociation. In this process one (or both) of the initial photons originates from the substructure of the nucleon, rather than from the exterior EM field of the whole nuclei. The photon interaction that produces the $e^+e^-$ pair is thus accompanied by the dissociation of the emitting nucleus, whose remnants are produced in the forward direction and are typically captured by the ZDC detector.

The contribution from dissociative events is estimated using a template fitting approach to the acoplanarity distribution. The signal template is simulated with STARLIGHT+PYTHIA8 and it is peaked at $\alpha \approx 0$, with some contribution in the tail originating from events with the FSR. The background template shape is taken from the single dissociative events simulated with SUPERCHIC v4.0 interfaced with PYTHIA8. These events have a much wider $\alpha$ distribution than the signal. The fit to the data is performed in the same intervals in $m_{ee}$ and $|y_{ee}|$ as in the study of the fractions of events in 0n0n, Xn0n and XnXn categories. In each bin, a binned maximum likelihood fitting procedure is performed separately in three ZDC categories. In the fit a normalisation of the relative background contribution, $f_{\text{bkg}}$, is taken to be a free parameter. The signal fraction is thus $(1 - f_{\text{bkg}})$. For the inclusive sample $f_{\text{bkg}}$ is a weighted sum of the results for 0n0n, Xn0n, and XnXn categories. The $f_{\text{bkg}}$ fraction accounts for contributions from dissociative and the exclusive ditau production, $\gamma\gamma \to \tau^+\tau^-$. The latter may contribute to the electron background, especially when both $\tau$-leptons decay in the electron channel. The ditau contribution is estimated using a dedicated MC sample from STARLIGHT. The resulting background fraction of $\gamma\gamma \to \tau^+\tau^-$ events in the full data sample amounts to 0.1%. It is found that the shape of the $\alpha$ distribution for the exclusive ditau events is similar to the $\alpha$ distribution for the pure dissociative component. However, the origin of this shape in ditau events is due to the presence of the neutrino in $\tau$-lepton decay. The dissociative contribution, $f_{\text{diss}}$, is therefore determined as the background fraction obtained from the fitting procedure, then reduced by the ditau background fraction.

The results of the fitting procedure on the data from the $10 < m_{ee} < 20$ GeV and $|y_{ee}| < 0.8$ interval are presented in Figure 3 for three ZDC categories as well as for the inclusive sample. The $f_{\text{bkg}}$ fraction amounts to $(0.3 \pm 0.2)\%$, $(9.9 \pm 0.6)\%$, $(13 \pm 1)\%$ and $(4.3 \pm 0.3)\%$ for the 0n0n, Xn0n, XnXn categories, and the inclusive sample, respectively.

The contribution from Upsilon production is estimated using the dedicated STARLIGHT+PYTHIA8 samples. Three Upsilon states, $\Upsilon(1S)$, $\Upsilon(2S)$, and $\Upsilon(3S)$ are considered. This background is significant only for $m_{ee}$ below 14 GeV and amounts to 2.4% of events passing the selecion criteria for the $\gamma\gamma \to e^+e^-$ process. The $\alpha$ distribution of the dielectron candidates from $\Upsilon$ decays is peaked at zero similar to the signal shape. It does not contribute to $f_{\text{bkg}}$ as the resulting fraction is not sensitive to 2.4% change in the acoplanarity peak.

A contribution to the background originating from photonuclear processes occuring in peripheral heavy ion collisions is largely suppressed by the trigger requirement in maximal deposited $E_{\text{T}}$ in the FCal. This assumption is also verified by examining the multiplicity distribution for Pixel-tracks. The number of events with more than two Pixel-tracks is equal to 1.3% and consistent with simulations of $\gamma\gamma \to e^+e^-$ events.
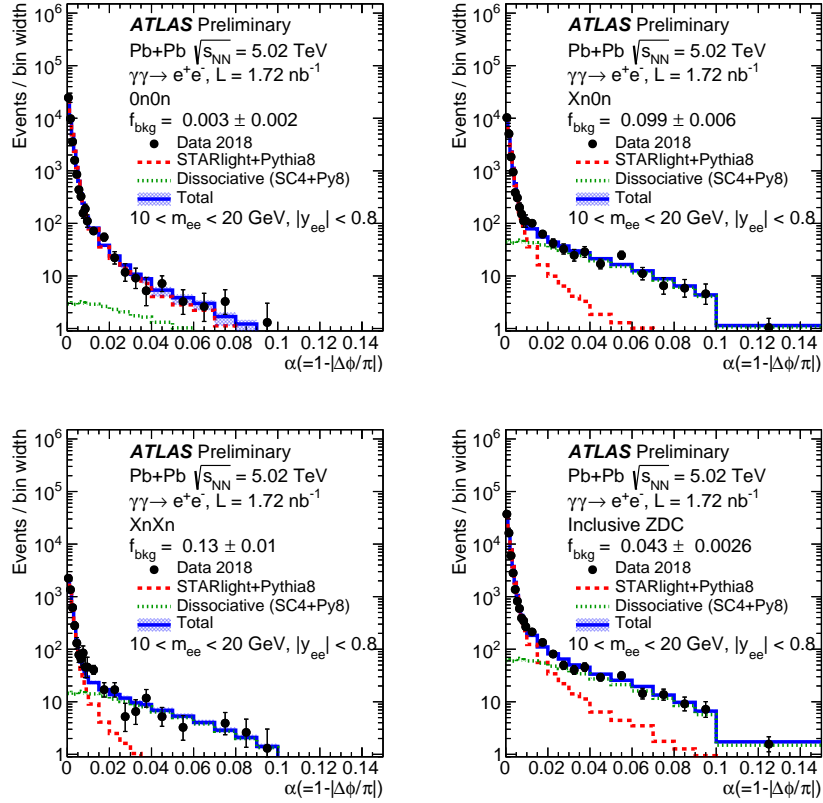
Figure 3: Acoplanarity distribution in the data sample (markers) of $\gamma\gamma \to e^+e^-$ candidates selected with $10 < m_{ee} <$ 20 GeV and $|y_{ee}| < 0.8$ requirements. The sample is split into 0n0n (top left), Xn0n (top right), XnXn (bottom left) and inclusive (bottom right) categories. A result of the fit of the dissociative background in each category is presented with the green dashed line while the prediction of the signal process is represented by the red line. A sum of the two components is also shown with the solid blue line. The resulting fraction of the background contribution to the data $f_{bkg}$ is given in the legend. The shaded area represents the total uncertainty on the sum of signal and background components.

Figure 4 shows control distributions for reconstructed and uncorrected values of $m_{ee}$, $\langle p_T^e \rangle$, $y_{ee}$, $|\cos\theta^*| = |\tanh(\frac{\Delta\eta_{ee}}{2})|$, and $\alpha$ for the inclusive data sample compared with MC predictions including the signal and background processes. In the MC, the trigger decision was not simulated. Instead, the distributions are weighted event-by-event by the parametrized trigger efficiency and by electron scale factors. The signal, Upsilon decay and ditau MC is normalized to the luminosity in data. The dissociative contribution was scaled to constitute the $f_{diss}$ fraction (determined for the inclusive sample) of the data. In general good agreement between data and the sum of the predictions for signal and background processes is found. On average the observed discrepancies are at the level of 10-15% with some exceptions which are discussed further. In the $m_{ee}$ distribution the data excess is more strongly pronounced for $m_{ee}$ between 10 and 20 GeV, where the difference between data and MC simulation is between 10 to 20%. The data to MC ratio drops below unity for masses above 40 GeV. The same features are observed in the $\langle p_T^e \rangle$ distribution with the largest deviations from unity in the range between 5–10 GeV. In the $y_{ee}$ distribution, the data excess is smaller, up to 10%, in the range from $-1.2$ to $1.2$, with rising discrepancies for larger $|y_{ee}|$ values. The data

to MC ratio in the $|\cos\theta^*|$ distribution drops slowly from 1.2 for $|\cos\theta^*| = 0$ to unity at $|\cos\theta^*| = 0.75$, and then falls more steeply, down to 0.5 for largest values of $|\cos\theta^*|$. In the $\alpha$ distribution, a difference in the overall shape is observed in the full range. This can be explained by a sensitivity of the results to the $p_T$ spectrum assumed by STARLIGHT, which determines the width of the $\alpha$ distribution. In general, all these discrepancies tend to be consistent with the observations established in the ATLAS $\gamma\gamma \rightarrow \mu^+\mu^-$ measurement [16] where the STARLIGHT predictions were found to underestimate the measured integrated fiducial cross-sections by about 10%.

# 6 Analysis

The integrated fiducial cross-section for exclusive dielectron production is calculated using the following formula:

$$\sigma^{\text{fid}} = \frac{N_{\text{data}} - N_{\text{bkg}}}{C \cdot A \cdot L}, \tag{1}$$

where:

- $N_{\text{data}}$ and $N_{\text{bkg}}$ refer to the number of events in data after event selection and the number of expected background events in this selected sample, respectively;

- $C$ is a correction factor accounting for detector inefficiencies (including the trigger), calculated as $N_{\text{MC,reco}}^{\text{fid,cut}}/N_{\text{MC,gen}}^{\text{fid,cut}}$ where $N_{\text{MC,gen}}^{\text{fid,cut}}$ is the number of generated events passing fiducial cuts of the analysis, while $N_{\text{MC,reco}}^{\text{fid,cut}}$ is the number of simulated signal events that also pass the reconstructed level selection;

- $A$ is the acceptance correction, used to correct the result for the exclusion of the calorimeter transition region and extrapolation from $|\eta^e| < 2.47$ to $|\eta^e| < 2.5$; and is calculated as $N_{\text{MC,gen}}^{\text{fid,cut}}/N_{\text{MC,gen}}^{\text{fid}}$, where $N_{\text{MC,gen}}^{\text{fid}}$ is the number of generated events passing all fiducial cuts of the analysis, except the calorimeter transition region exclusion cut;

- $L$ is the total integrated luminosity.

Both $N_{\text{MC,gen}}^{\text{fid,cut}}$ and $N_{\text{MC,gen}}^{\text{fid}}$ are extracted with respect to the generated-level electrons before the FSR. The fiducial region is defined by the following requirements: $p_T^e > 2.5$ GeV, $|\eta^e| < 2.5$, $m_{ee} > 5$ GeV, and $p_T^{ee} < 2$ GeV. The number of events passing the fiducial selection is $N_{\text{data}} = 30456$. The dissociative and ditau background fraction obtained from the fit amounts to 4.5%. The Upsilon background amounts to 2.4% of all events passing the selecion criteria.

The selected data sample is corrected in a few subsequent steps in order to compare it with the theoretical predictions. As a first step the backgrounds are subtracted. Distributions in the data are reweighted event-by-event by the factor $(1 - f_{\text{bkg}})$ where $f_{\text{bkg}}$ is the fraction of background (inclusive in ZDC) from the fit in a given $m_{ee}$ and $|y_{ee}|$ range. For masses above 40 GeV, the fraction obtained from the fit in the full $|y_{ee}| < 2.4$ range is taken. For events with $m_{ee}$ below 40 GeV, the fraction as a function of $|y_{ee}|$ is used. If $|y_{ee}|$ exceeds 2.4, the fraction from the $1.6 < |y_{ee}| < 2.4$ bin is applied. In the next step, the background expected from $\Upsilon(\text{nS})$ decays is subtracted.

For differential cross-section measurement, the data is corrected with fiducial correction factors defined as the fraction of events in each bin which fall into the fiducial region on the generated level. These factors correct for the events that are reconstructed to be within the fiducial region, but fall outside it at generated
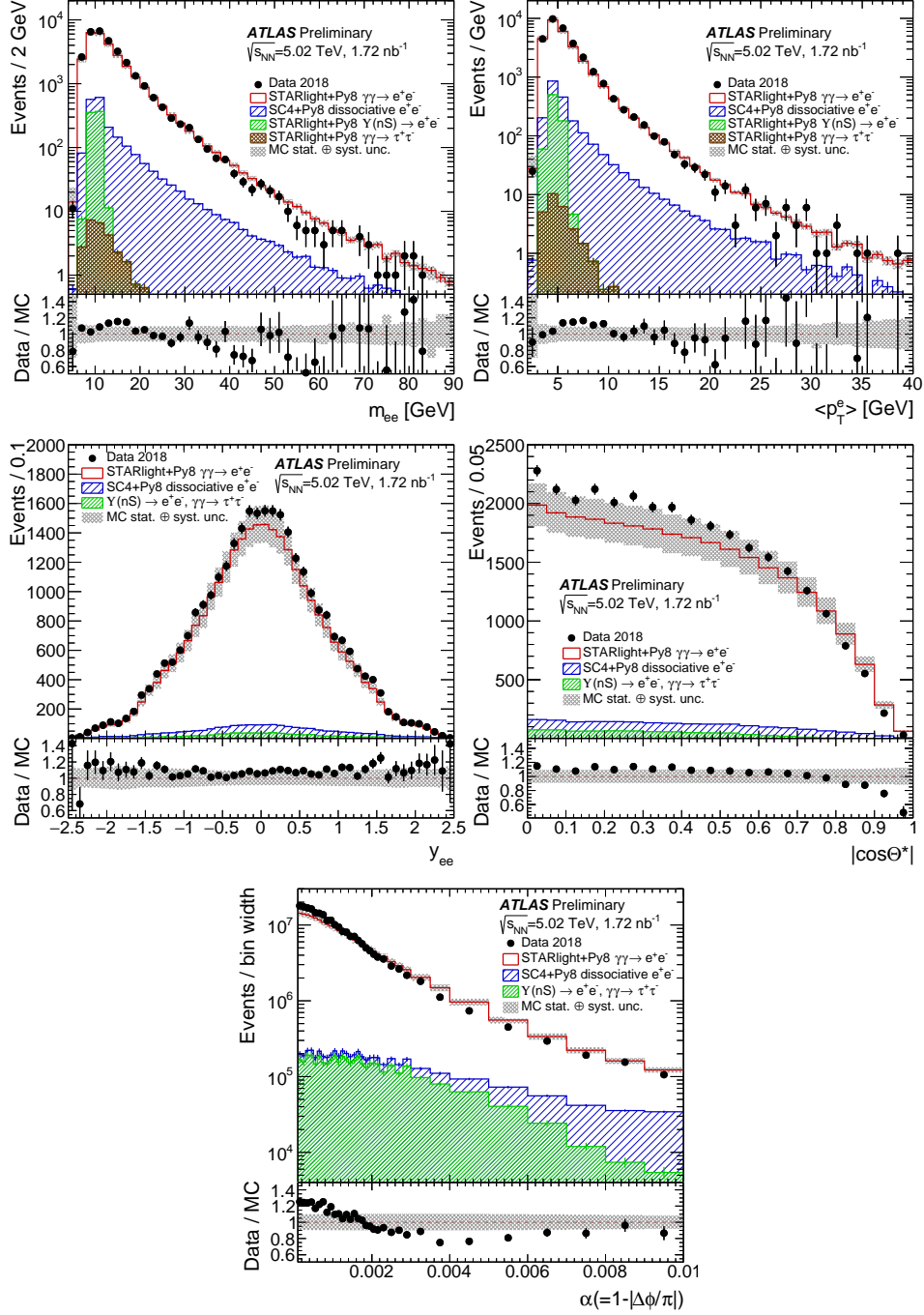
Figure 4: Distributions of $m_{ee}$ (top left), $\langle p_T^e \rangle$ (top right), $y_{ee}$ (middle left), $|\cos\theta^*|$ (middle right), and $\alpha$ (bottom) for the inclusive sample in data and MC predictions for signal and background processes. Ratio panels present data over MC simulation. Error bars represent statistical uncertainties. The shaded area represents the total uncertainty on the total MC prediction. In $y_{ee}$, $|\cos\theta^*|$, and $\alpha$ distributions Upsilon and ditau contributions are shown together.

level. They are parametrised using the reconstructed kinematic variables. They deviate from unity at the subpercent level, therefore their impact is marginal. After this, the reconstructed data are unfolded

using the bayesian inspired iterative procedure [42] with one iteration for all distributions implemented in the RooUnfold package [43], using response matrices derived from signal MC samples. The number of iterations is chosen to minimise the resulting statistical uncertainty and at the same time to provide a good closure. A closure test based on the signal MC samples is performed to verify the unfolding procedure. The signal sample is split into two parts. The first part is used to fill the response matrices, while the second one is unfolded. The ratio of the unfolded yields to the generated yields deviates from unity by 1% at most.

Finally, the distributions are divided by the luminosity as well as the product of correction factors, $C \times A$, which account for detector inefficiencies as well as acceptance losses. They are determined for each bin of the unfolded distribution as the fraction of events that pass the fiducial requirements for reconstructed level, in events that pass them for generated level. The $C \times A$ factors are parametrised using generated-level kinematics, but then weighed by trigger and reconstruction efficiency scale factors, evaluated at reconstructed scale. The average $C$ and $A$ factors amount to 0.087 and 0.878, respectively.

# 7  Systematic uncertainties

In the cross-section measurement the following systematic uncertainties are considered. The total scale factors for the electron reconstruction and identification efficiency [38] are varied up and down coherently over the full kinematic range, as a conservative estimate. The data-driven trigger efficiency, which is the product of the Level-1 efficiency, the Pixel-veto efficiency, and the forward transverse energy requirement efficiency, is varied up and down by its total uncertainty. To assess known uncertainties in the EM energy scale and energy resolution, the calibrations are varied with factors determined in 13 TeV $pp$ collisions [38]. The uncertainties related to the background contributions are varied up and down by their total uncertainties. The dissociative backgrounds are dominated by their statistical uncertainties from the fit. The systematic uncertainties are also evaluated, with the largest contribution related to the shape of the signal template. This is estimated using data from 0n0n category as a signal distribution for Xn0n and XnXn categories. The background template shape uncertainty is estimated by adding the double dissociative component. The uncertainty on the expected Upsilon yields is dominated by both the efficiency scale factors and the EM energy scale.

For the differential cross-sections, additional systematic uncertainties are related to the unfolding procedures. The MC sample is split in two, with one subsample used to determine the response matrix and the other treated as a simulated dataset. The differences between the generated and unfolded yields are treated as a systematic uncertainty. Similarly, the sensitivity to the Bayesian prior is tested by reweighing the simulated dataset to agree with the reconstructed data. Again, the differences between simulated and reconstructed yields in this closure test are applied as an uncertainty. While the primary unfolding is evaluated in one dimension rather than two, a cross check is performed using the 2D response. Resulting two-dimensional cross-sections are projected to one dimension and compared with the nominal results. The small differences are included as a separate uncertainty. Finally, the spectra are evaluated in the 0n0n category, using the fractions determined in Section 4, but evaluated for generator-level $m_{ee}$ and $|y_{ee}|$ (as opposed to the reconstructed values). The differences are found to be within 1–2%.

The uncertainty in the integrated luminosity of the data sample is 2.0%. It is derived from the calibration of the luminosity scale using $x$-$y$ beam-separation scans, following a methodology similar to that detailed in Ref. [44], and using the LUCID-2 detector for the baseline luminosity measurements [45].

A summary of the systematic uncertainties as a function of $m_{ee}$ and $|y_{ee}|$ is shown in Figure 5. The dominant source of uncertainty arises from the uncertainties on the electron scale factors. They are at the level of 10–11% in the whole range of $m_{ee}$, and they rise from 9% at $|y_{ee}| \approx 0$ to about 15% at $|y_{ee}|$ close to 2. The systematic uncertainty from the trigger efficiency is approximately 2% for $m_{ee}$ above 10 GeV and $|y_{ee}|$ below 1.6. They rise up to 4% for smaller $m_{ee}$, and up to 6% for highest $|y_{ee}|$. The uncertainty related to the energy scale and resolution is below 1% in the whole range of $|y_{ee}|$, but exceeds this value in some $m_{ee}$ bins, up to approximately 5% for lowest $m_{ee}$. The background uncertainties are within 1–3% and slightly increase with $m_{ee}$ and $|y_{ee}|$. Uncertainties related to unfolding procedures do not exhibit such clear dependencies in $m_{ee}$ and $|y_{ee}|$. They are mostly within the 2–3% range but exceed this value, up to 5%, at intermediate $m_{ee}$ and small $|y_{ee}|$.
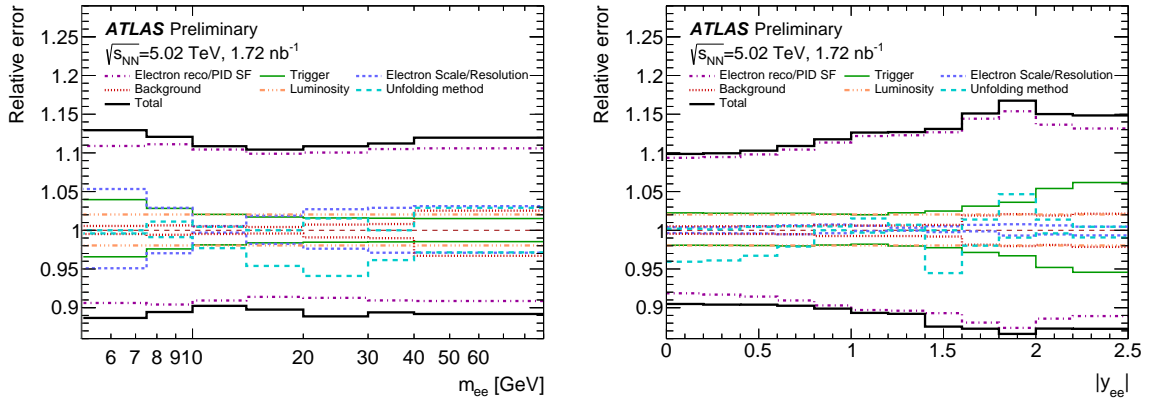


Figure 5: Breakdown of relative systematic uncertainties on the differential cross-section as a function of $m_{ee}$ (left) and $|y_{ee}|$ (right).

# 8 Results

The total integrated fiducial cross-section is measured to be $215 \pm 1$ (stat.) $^{+23}_{-20}$ (syst.) $\pm 4$ (lumi.) $\mu$b. The STARLIGHT prediction for the total integrated fiducial cross-section is 196.9 $\mu$b, while the SUPERCHIC prediction is 235.1 $\mu$b. Both predictions are statistically compatible with the measurement.

The differential cross-sections for exclusive dielectron production are presented as a function of $m_{ee}$, $\langle p_T^e \rangle$, $|y_{ee}|$, and $|\cos\theta^*|$ in Figure 6. The cross-sections are measured inclusive in the ZDC selection. The results are corrected for detector inefficiency and resolution effects, and are compared to STARLIGHT and SUPERCHIC v3.05 predictions for the signal $\gamma\gamma \to e^+e^-$ process. The bottom panel on each plot shows the ratio between the unfolded data and MC predictions. On average the STARLIGHT predictions underestimate the data by about 10–15% while SUPERCHIC predictions are higher by about the same amount. Both predictions tend to have very similar shapes. The difference in the absolute normalisation of the two predictions is due to different approach in the implementation of the non-hadronic overlap condition of the Pb ions. The predictions describe the shape of the data well, except at high $|y_{ee}|$ and high $|\cos\theta^*|$. The differences are more pronounced for $m_{ee}$ between 10 and 20 GeV, and for $\langle p_T^e \rangle$ between 5 and 10 GeV. The ratio to STARLIGHT rises from about 1.1 to 1.2 when increasing $|y_{ee}|$ from 0 to 2.5. For $|\cos\theta^*|$ close to 0, the data to STARLIGHT ratio is the largest, around 1.15, then it slowly decreases to about 1.05 for

$|\cos\theta^*| = 0.8$. The ratio falls more steeply in the last two bins of $|\cos\theta^*|$ and drops below unity to 0.75 and 0.65 for STARLIGHT and SUPERCHIC respectively. The deficit in measured cross-sections over the theory predictions is 1.8 (2.7) standard deviations for STARLIGHT (SUPERCHIC) at the highest $|\cos\theta^*|$ bin. There is a plausible proposal available for the relevance of higher-order scattering processes (involving more than two photons in the initial state) which tends to reduce the predicted cross-sections by the observed amount [46].
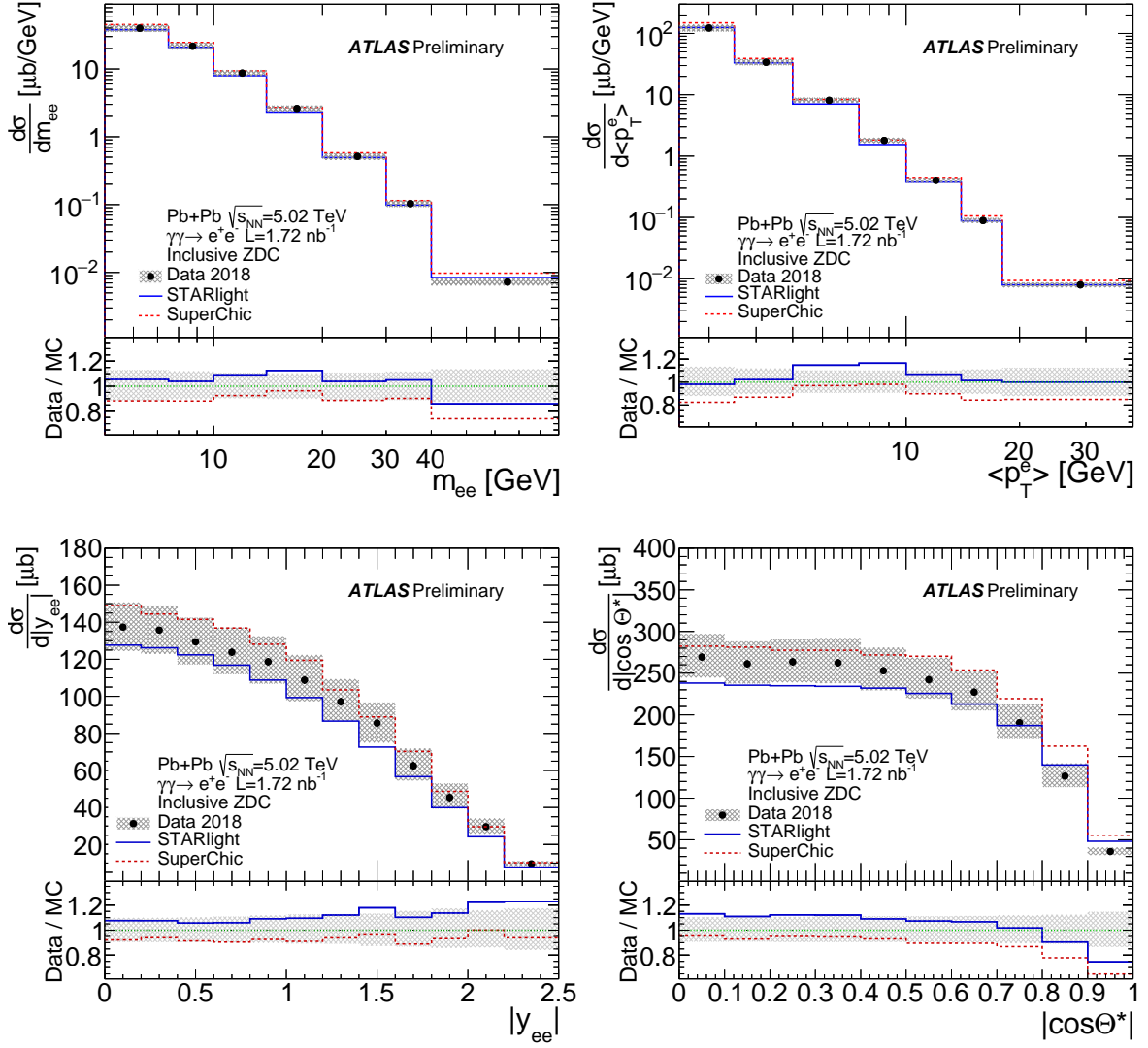


Figure 6: Fully corrected differential cross-sections measured inclusive in the ZDC for exclusive dielectron production, $\gamma\gamma \to e^+e^-$, as a function of $m_{ee}$, $\langle p_T^e \rangle$, $|y_{ee}|$ and $|\cos\theta^*|$ for data (dots) and MC predictions from STARLIGHT (solid blue) and SUPERCHIC (dashed red). Bottom panels present a ratio of data over MC predictions. The shaded area represents the total uncertainty on the data excluding the 2% luminosity uncertainty.

The differential cross-sections as a function of $m_{ee}$, $\langle p_T^e \rangle$, $|y_{ee}|$ and $|\cos\theta^*|$ for the 0n0n category are presented in Figure 7. They are compared with the MC predictions from STARLIGHT and SUPERCHIC v3.05. Both simulated samples were produced inclusively and reweighed to the 0n0n category using the measured

fractions in the inclusive data sample. Each theory prediction is represented by two curves reflecting the systematic variations on the measured 0n0n fractions. STARLIGHT can also generate a prediction conditional on the presence of neutron emission in one or both directions. These dedicated predictions from STARLIGHT for the 0n0n category are shown in the same plots. That prediction matches well the shape of the inclusive STARLIGHT prediction corrected for the measured 0n0n fractions but is systematically lower by 2–3% for $|y_{ee}| < 1.4$. The general conclusions from this comparison between MC predictions and data are consistent with the inclusive case. The agreement between data and MC is generally better for lower $|y_{ee}|$ and $|\cos\theta^*|$ values, i.e. involving lower energy initial-state photons.
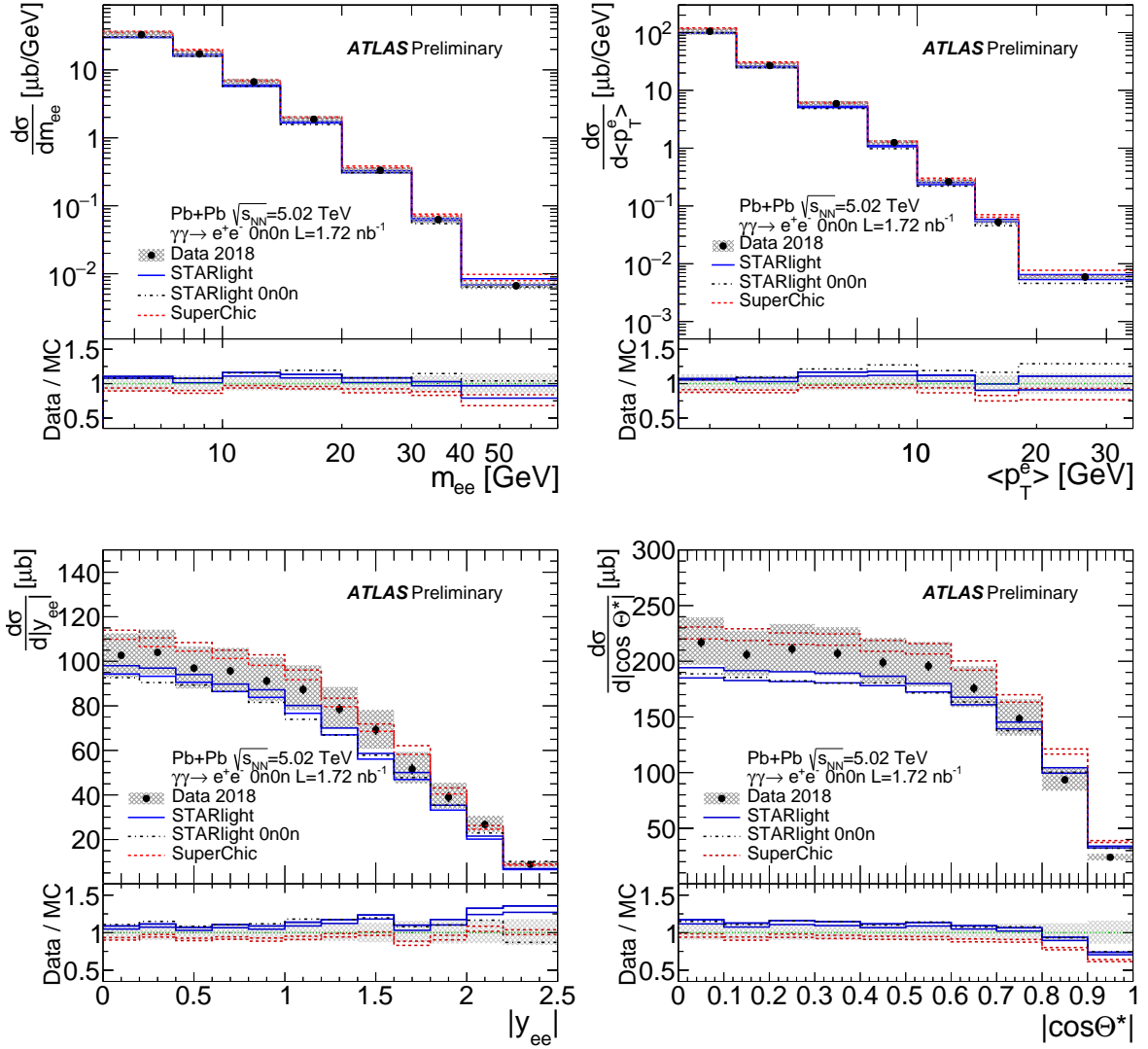


Figure 7: Fully corrected differential cross-sections measured for the 0n0n category for exclusive dielectron production as a function of $m_{ee}$, $\langle p_T^e \rangle$, $|y_{ee}|$ and $|\cos\theta^*|$. The cross-sections are compared to MC predictions from STARLIGHT (solid blue) and SUPERCHIC v3.05 (dashed red) represented by two lines reflecting systematic variations. Also a dedicated prediction from STARLIGHT for the 0n0n category (dashed-dotted black) is shown. A ratio panel shows data over predictions. The shaded area represents the total uncertainty on the data excluding the 2% luminosity uncertainty.

# 9 Conclusions

A measurement of the cross-section for exclusive dielectron production, $\gamma\gamma \to e^+e^-$, was performed using $\mathcal{L}_{int}$ = 1.72 nb$^{-1}$ of ultraperipheral Pb+Pb collision data at $\sqrt{s_{NN}}$ = 5.02 TeV recorded by the ATLAS detector at the LHC. The cross-section is corrected for detector efficiency, acceptance losses, and background contributions. The backgrounds from dissociative processes, Upsilon decays, and ditau production were subtracted, with the former estimated using a template fit to the acoplanarity distribution. After all corections, the integrated cross-section for the $\gamma\gamma \to e^+e^-$ process in the fiducial region, defined by $p_T^e$ > 2.5 GeV, $|\eta^e|$ < 2.5, $m_{ee}$ > 5 GeV, and $p_T^{ee}$ < 2 GeV requirements, is measured to be 215 ±1 (stat.) $^{+23}_{-20}$ (syst.) ±4 (lumi.) $\mu$b. Within experimental uncertainties the data are in good agreement with the QED predictions from Starlight and SuperChic v3.05. The differential cross-sections are presented as a function of $m_{ee}$, $\langle p_T^e \rangle$, $|y_{ee}|$ and $|\cos\theta^*|$, both with and without requirements on forward neutron activity. The differential results are compared with the prediction from Starlight v313 and SuperChic v3.05. In general a good agreement is found in the shapes of the distributions, however some systematic differences occur. In particular, the discrepancy between the data and Starlight prediction rises with higher $|y_{ee}|$, similar to what was observed with $\gamma\gamma \to \mu^+\mu^-$ [16]. For $|\cos\theta^*| \approx 1$ the deficit in measured cross-sections over the theory predictions amounts to 1.8 (2.7) standard deviations for Starlight (SuperChic). The agreement between data and MC is generally better for lower $|y_{ee}|$ and $|\cos\theta^*|$ values.

# References

[1]  A. Baltz et al., *The physics of ultraperipheral collisions at the LHC*, Physics Reports **458** (2008) 1,
     issn: 0370-1573,
     url: https://www.sciencedirect.com/science/article/pii/S0370157307004462
     (cit. on p. 2).

[2]  S. Klein and P. Steinberg,
     *Photonuclear and Two-photon Interactions at High-Energy Nuclear Colliders*,
     Ann. Rev. Nucl. Part. Sci. **70** (2020) 323, arXiv: 2005.01872 [nucl-ex] (cit. on p. 2).

[3]  E. Fermi, *On the theory of collisions between atoms and electrically charged particles*,
     Nuovo Cim. **2** (1925) 143, arXiv: hep-th/0205086 [hep-th] (cit. on p. 2).

[4]  E. J. Williams, *Nature of the High Energy Particles of Penetrating Radiation and Status of
     Ionization and Radiation Formulae*, Phys. Rev. **45** (10 1934) 729 (cit. on p. 2).

[5]  G. Breit and J. A. Wheeler, *Collision of Two Light Quanta*, Phys. Rev. **46** (12 1934) 1087
     (cit. on p. 2).

[6]  A. Veyssiere, H. Beil, R. Bergere, P. Carlos and A. Lepretre,
     *Photoneutron cross sections of $^{208}Pb$ and $^{197}Au$*, Nuclear Physics A **159** (1970) 561,
     issn: 0375-9474,
     url: https://www.sciencedirect.com/science/article/pii/037594747090727X
     (cit. on p. 2).

[7]  ATLAS Collaboration, *Measurement of exclusive $\gamma\gamma \to \ell^+\ell^-$ production in proton-proton
     collisions at $\sqrt{s}$ = 7 TeV with the ATLAS detector*, Phys. Lett. B **749** (2015) 242,
     arXiv: 1506.07098 [hep-ex] (cit. on p. 3).

[8] CMS Collaboration,
*Search for Exclusive or Semi-Exclusive Photon Pair Production and Observation of Exclusive and Semi-Exclusive Electron Pair Production in pp Collisions at $\sqrt{s}$ = 7 TeV*, JHEP **11** (2012) 080, arXiv: 1209.1666 [hep-ex] (cit. on p. 3).

[9] CMS Collaboration,
*Exclusive photon-photon production of muon pairs in proton-proton collisions at $\sqrt{s}$ = 7 TeV*, JHEP **01** (2012) 052, arXiv: 1111.5536 [hep-ex] (cit. on p. 3).

[10] ATLAS Collaboration, *Measurement of the exclusive $\gamma\gamma \to \mu^+\mu^-$ process in proton-proton collisions at $\sqrt{s}$ = 13 TeV with the ATLAS detector*, Phys. Lett. B **777** (2018) 303, arXiv: 1708.04053 [hep-ex] (cit. on p. 3).

[11] ATLAS Collaboration, *Observation and Measurement of Forward Proton Scattering in Association with Lepton Pairs Produced via the Photon Fusion Mechanism at ATLAS*, Phys. Rev. Lett. **125** (2020) 261801, arXiv: 2009.14537 [hep-ex] (cit. on p. 3).

[12] CMS and TOTEM Collaborations,
*Observation of proton-tagged, central (semi)exclusive production of high-mass lepton pairs in pp collisions at 13 TeV with the CMS-TOTEM precision proton spectrometer*, JHEP **07** (2018) 153, arXiv: 1803.04496 [hep-ex] (cit. on p. 3).

[13] ALICE Collaboration, *Charmonium and $e^+e^-$ pair photoproduction at mid-rapidity in ultra-peripheral Pb-Pb collisions at $\sqrt{s_{NN}}$=2.76 TeV*, Eur. Phys. J. C **73** (2013) 2617, arXiv: 1305.1467 [nucl-ex] (cit. on p. 3).

[14] STAR Collaboration, *Low-$p_T$ $e^+e^-$ pair production in Au+Au collisions at $\sqrt{s_{NN}}$ = 200 GeV and U+U collisions at $\sqrt{s_{NN}}$ = 193 GeV at STAR*, Phys. Rev. Lett. **121** (2018) 132301, arXiv: 1806.02295 [hep-ex] (cit. on p. 3).

[15] STAR Collaboration, *Measurement of $e^+e^-$ Momentum and Angular Distributions from Linearly Polarized Photon Collisions*, Phys. Rev. Lett. **127** (2021) 052302, arXiv: 1910.12400 [nucl-ex] (cit. on p. 3).

[16] ATLAS Collaboration,
*Exclusive dimuon production in ultraperipheral Pb+Pb collisions at $\sqrt{s_{NN}}$ = 5.02 TeV with ATLAS*, Phys. Rev. C **104** (2021) 024906, arXiv: 2011.12211 [nucl-ex] (cit. on pp. 3, 6, 10, 16).

[17] ATLAS Collaboration, *Observation of centrality-dependent acoplanarity for muon pairs produced via two-photon scattering in Pb+Pb collisions at $\sqrt{s_{NN}}$ = 5.02 TeV with the ATLAS detector*, Phys. Rev. Lett. **121** (2018) 212301, arXiv: 1806.08708 [nucl-ex] (cit. on p. 3).

[18] CMS Collaboration, *Observation of Forward Neutron Multiplicity Dependence of Dimuon Acoplanarity in Ultraperipheral Pb-Pb Collisions at $\sqrt{s_{NN}}$=5.02 TeV*, Phys. Rev. Lett. **127** (2021) 122001, arXiv: 2011.05239 [hep-ex] (cit. on p. 3).

[19] M. Dyndał, M. Kłusek-Gawenda, A. Szczurek and M. Schott, *Anomalous electromagnetic moments of $\tau$ lepton in $\gamma\gamma \to \tau^+\tau^-$ reaction in Pb+Pb collisions at the LHC*, Physics Letters B **809** (2020) 135682, ISSN: 0370-2693 (cit. on p. 3).

[20] L. Beresford and J. Liu, *New physics and tau $g - 2$ using LHC heavy ion collisions*, Phys. Rev. D **102** (11 2020) 113008, URL: https://link.aps.org/doi/10.1103/PhysRevD.102.113008 (cit. on p. 3).

[21] ATLAS Collaboration,
*Evidence for light-by-light scattering in heavy-ion collisions with the ATLAS detector at the LHC*,
Nature Phys. **13** (2017) 852, arXiv: 1702.01625 [hep-ex] (cit. on p. 3).

[22] ATLAS Collaboration, *Observation of light-by-light scattering in ultraperipheral Pb+Pb collisions with the ATLAS detector*, Phys. Rev. Lett. **123** (2019) 052001, arXiv: 1904.03536 [hep-ex]
(cit. on p. 3).

[23] ATLAS Collaboration, *Measurement of light-by-light scattering and search for axion-like particles with 2.2 nb$^{-1}$ of Pb+Pb data with the ATLAS detector*, JHEP **11** (2021) 050,
arXiv: 2008.05355 [hep-ex] (cit. on p. 3).

[24] CMS Collaboration, *Evidence for light-by-light scattering and searches for axion-like particles in ultraperipheral PbPb collisions at $\sqrt{s_{NN}}$ = 5.02 TeV*, Phys. Lett. B **797** (2019) 134826,
arXiv: 1810.04602 [hep-ex] (cit. on p. 3).

[25] ATLAS Collaboration, *The ATLAS experiment at the CERN Large Hadron Collider*,
JINST **3** (2008) S08003 (cit. on p. 3).

[26] ATLAS Collaboration, *ATLAS Insertable B-Layer Technical Design Report*, (2010),
URL: https://cds.cern.ch/record/1291633 (cit. on p. 4).

[27] ATLAS Collaboration, *Performance of the ATLAS Trigger System in 2015*,
Eur. Phys. J. C **77** (2017) 317, arXiv: 1611.09661 [hep-ex] (cit. on p. 4).

[28] ATLAS Collaboration, *Operation of the ATLAS trigger system in Run 2*, JINST **15** (2020) P10004,
arXiv: 2007.12539 [hep-ex] (cit. on p. 4).

[29] ATLAS Collaboration, *The ATLAS Collaboration Software and Firmware*,
ATL-SOFT-PUB-2021-001, 2021, URL: https://cds.cern.ch/record/2767187
(cit. on pp. 4, 5).

[30] ATLAS Collaboration, *ATLAS data quality operations and performance for 2015–2018 data-taking*,
JINST **15** (2020) P04003, arXiv: 1911.04632 [physics.ins-det] (cit. on p. 4).

[31] S. R. Klein, J. Nystrand, J. Seger, Y. Gorbunov and J. Butterworth,
*STARlight: A Monte Carlo simulation program for ultra-peripheral collisions of relativistic ions*,
Comput. Phys. Commun. **212** (2017) 258, arXiv: 1607.03838 [hep-ph] (cit. on p. 4).

[32] M. L. Miller, K. Reygers, S. J. Sanders and P. Steinberg,
*Glauber Modeling in High-Energy Nuclear Collisions*,
Annual Review of Nuclear and Particle Science **57** (2007) 205,
URL: https://doi.org/10.1146/annurev.nucl.57.090506.123020 (cit. on p. 5).

[33] L. A. Harland-Lang, V. A. Khoze and M. G. Ryskin,
*Exclusive LHC physics with heavy ions: SuperChic 3*,
The European Physical Journal C **79** (2019) 39,
URL: https://doi.org/10.1140/epjc/s10052-018-6530-5 (cit. on p. 5).

[34] T. Sjöstrand et al., *An introduction to PYTHIA 8.2*, Comput. Phys. Commun. **191** (2015) 159,
arXiv: 1410.3012 [hep-ph] (cit. on p. 5).

[35] L. A. Harland-Lang, M. Tasevsky, V. A. Khoze and M. G. Ryskin, *A new approach to modelling elastic and inelastic photon-initiated production at the LHC: SuperChic 4*,
Eur. Phys. J. C **80** (2020) 925, arXiv: 2007.12704 [hep-ph] (cit. on p. 5).

[36] GEANT4 Collaboration, S. Agostinelli et al., *GEANT4: A Simulation toolkit*,
Nucl. Instrum. Meth. **A506** (2003) 250 (cit. on p. 5).

[37] ATLAS Collaboration, *The ATLAS Simulation Infrastructure*, Eur. Phys. J. **C70** (2010) 823,
arXiv: 1005.4568 [physics.ins-det] (cit. on p. 5).

[38] ATLAS Collaboration, *Electron and photon performance measurements with the ATLAS detector using the 2015–2017 LHC proton-proton collision data*, JINST **14** (2019) P12006,
arXiv: 1908.00005 [hep-ex] (cit. on pp. 5, 7, 12).

[39] ATLAS Collaboration,
*Early Inner Detector Tracking Performance in the 2015 Data at $\sqrt{s}$ = 13 TeV*,
ATL-PHYS-PUB-2015-051, 2015, URL: https://cds.cern.ch/record/2110140 (cit. on p. 6).

[40] ATLAS Collaboration,
*Performance of the ATLAS track reconstruction algorithms in dense environments in LHC Run 2*,
Eur. Phys. J. C **77** (2017) 673, arXiv: 1704.07983 [hep-ex] (cit. on p. 6).

[41] ALICE Collaboration, B. Abelev et al., *Measurement of the Cross Section for Electromagnetic Dissociation with Neutron Emission in Pb-Pb Collisions at $\sqrt{s_{NN}}$ = 2.76 TeV*,
Phys. Rev. Lett. **109** (2012) 252302, arXiv: 1203.2436 [nucl-ex] (cit. on p. 6).

[42] G. D'Agostini, *A multidimensional unfolding method based on Bayes' theorem*,
Nuclear Instruments and Methods in Physics Research Section A: Accelerators, Spectrometers, Detectors and Associated Equipment **362** (1995) 487, ISSN: 0168-9002,
URL: https://www.sciencedirect.com/science/article/pii/016890029500274X
(cit. on p. 12).

[43] T. Adye, 'Unfolding algorithms and tests using RooUnfold',
*Proceedings, 2011 Workshop on Statistical Issues Related to Discovery Claims in Search Experiments and Unfolding (PHYSTAT 2011)* (CERN, Geneva, Switzerland, 17th–20th Jan. 2011) 313, arXiv: 1105.1160 [physics.data-an] (cit. on p. 12).

[44] ATLAS Collaboration,
*Luminosity determination in pp collisions at $\sqrt{s}$ = 8 TeV using the ATLAS detector at the LHC*,
Eur. Phys. J. C **76** (2016) 653, arXiv: 1608.03953 [hep-ex] (cit. on p. 12).

[45] G. Avoni et al., *The new LUCID-2 detector for luminosity measurement and monitoring in ATLAS*,
JINST **13** (2018) P07017 (cit. on p. 12).

[46] W. Zha and Z. Tang,
*Discovery of higher-order quantum electrodynamics effect for the vacuum pair production*,
JHEP **08** (2021) 083, arXiv: 2103.04605 [hep-ph] (cit. on p. 14).